PERGAMON

International Journal of Heat and Mass Transfer 43 (2000) 457–471

International Journal of HEAT and MASS TRANSFER

www.elsevier.com/locate/ijhmt

Flow and heat transfer characteristics of backward-facing step laminar flow in a rectangular duct

Hiroshi Iwai*, Kazuyoshi Nakabe, Kenjiro Suzuki

Department of Mechanical Engineering, Kyoto University, Kyoto 606-8501, Japan

Received 18 September 1998; received in revised form 11 March 1999

Abstract

Three-dimensional numerical simulation has been performed for flows over a backward-facing step at low Reynolds number in order to investigate the effects of the duct aspect ratio. Numerical results were compared with other investigations and found to agree well with experimental data. Close attention was paid to the distribution patterns of both Nusselt number and the skin friction coefficient on the bottom wall. It was found that an aspect ratio of as large as $AR = 16$ at least was needed to obtain a 2D region near the centerline at $Re = 250$. This 2D region became wider for a lower Reynolds number. It was also found that the maximum Nusselt number did not appear on the centerline but near the two side walls in every case.

Keywords: 3-D simulation; Backward-facing step; Low Reynolds number; Aspect ratio

1. Introduction

Recent requirement for the downsizing of heat exchanger brought the Reynolds number of the flows inside the heat exchangers relatively low. When Reynolds number is low enough, the flows become laminar. Heat transfer enhancement due to the turbulence cannot be expected under such conditions. In order to establish a favorable heat exchange at low Reynolds number, it is necessary to modify the flow structure appropriately, for instance, with vortex generators [1,2] or ribs [3,4]. Such flow modification often includes the flow separation and reattachment. Consequently, the modified flows tend to have quite complicated flow structures. In order to improve the performance of heat exchangers, understanding the details of such complicated flow structures is very important. Therefore, attention has been paid to one of the flows in such category, namely a separating and reattaching flow. In particular, as the most typical problem, backward-facing step flows under laminar conditions have been investigated both experimentally [5–8] and numerically [9–13] to obtain the basic information of the flow separation and reattachment phenomena in laminar flow regime.

In most of the experimental investigations, a considerably large aspect ratio of the duct was adopted in order to assume the two-dimensionality of the flow around the duct center region. Armaly et al. [7] adopted the duct aspect ratio of 36 and ensured that the oncoming flow was two-dimensional (2D). He measured quite successfully the distributions of the streamwise velocity for backward-facing step flows in a wide Reynolds number range, including laminar cases, using Laser-Doppler anemometer. Nevertheless, it was reported in his paper that the flow downstream of the step remained 2D only at $Re < 200$ and $Re > 3000$.

* Corresponding author. Tel.: +81-75-753-5218; fax: +81-75-771-7286.

E-mail address: iwai@htrans.mech.kyoto-u.ac.jp (H. Iwai)

0017-9310/00/$ - see front matter
PII: S0017-9310(99)00140-4

Nomenclature

AR	aspect ratio $= WD/S$
C_f	streamwise skin friction coefficient $= 2\tau_w/\rho U_{in}^2$
C_P	specific heat
C_p	pressure coefficient $= 2\Delta P/\rho U_{in}^2$
$C_{p,z}$	non-dimensional pressure non-uniformity $= 2\Delta P/\rho U_{in}^2$
ER	duct expansion ratio $= H/(H-S)$
H	duct height
h	enthalpy
Nu	Nusselt number $= q_w S/\lambda(T_w - T_{in})$
P	pressure
q	heat flux
Re	Reynolds number $= \rho U_{in} S/\mu$
S	step height
T	temperature
T_{in}	inlet temperature
t	time
U	velocity component in x-direction
U_{in}	cross-sectional mean velocity at the inlet
V	velocity component in y-direction
W	velocity component in z-direction
WD	duct width
Wy	spanwise skin friction coefficient
x	streamwise coordinate
y	transverse coordinate
z	spanwise coordinate
λ	thermal conductivity
μ	fluid viscosity
ρ	density
τ	shear stress $= \mu(\partial U/\partial y)$

Subscripts

m	mean value in a cross-section
max	maximum Nusselt number and its position
r	reattachment point
w	wall surface

In numerical calculation the flows are often assumed to be 2D, since 2D simulations require less CPU time and consume less memory compared with 3D simulations. Although 2D simulation is useful to obtain the basic idea of the flow and thermal fields, it is reported that the results of the 2D computations sometimes show larger discrepancy from the experimental results as Reynolds number is increased, even in its range where the flow remains laminar [7–11]. This discrepancy is claimed to be a result of 3D flow structures in experiments. Kaiktsis et al. [11] performed 3D simulations employing periodic boundary condition in the spanwise direction. However, his numerical results still show noticeable discrepancy from the experimental results. One of the possible reason for this discrepancy is the 3D structure of flow and thermal fields due to the existence of side walls.

In this study, 3D numerical computation is performed for both flow and thermal fields over a backward-facing step in a rectangular duct in order to investigate the 3D side wall effects on the flow and thermal fields.

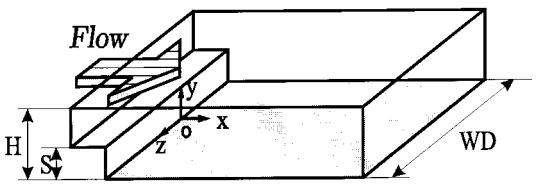

Fig. 1. Computational domain.

2. Computational method

The computational domain is schematically illustrated in Fig. 1. The duct is made up of a stepped wall, a straight wall and two side walls. The origin of the coordinate system is located at the center of the bottom line of the backward-facing wall. The computational domain is set to cover the streamwise positions of $-1 \le x/S \le 30$, where S is the step height. It was confirmed that the effects of domain size on final results were small enough with this arrangement for the computational domain. The duct expansion ratio, $ER = H/(H-S)$, is kept constant at two. Unsteady Navier–Stokes and energy equations are solved numerically together with the continuity equation using the finite difference method.

$$\frac{\partial \rho}{\partial t} + \nabla \cdot \left(\rho \vec{U}\right) = 0 \tag{1}$$

$$\frac{\partial}{\partial t}\left(\rho \vec{U}\right) + \nabla\left(\rho \vec{U}\vec{U}\right) = -\nabla P + \mu \nabla^2 \vec{U} \tag{2}$$

$$\frac{\partial}{\partial t}(\rho h) + \nabla \cdot \left(\rho \vec{U} h\right) = \nabla \cdot \left(\frac{\lambda}{C_P} \nabla h\right) \tag{3}$$

U, V, W, which will be used hereafter instead of $\vec{U}$, stand for velocity components in x-, y- and z-direction, respectively. A fifth-order upwind scheme and a fourth-order central difference scheme are adopted for the convection and diffusion terms of the governing

Table 1
Computational conditions

AR	$Re = 125$	$Re = 250$	$Re = 300$	$Re = 375$
4		○		
8		○		
16	○	○	○	○
24		○		

equations, respectively. Properties of the working fluid (air) are assumed to be constant. This implies that the fluid is incompressible and the first term in Eq. (1) is zero. Prandtl number is set at 0.71. The obtained fully implicit forms of the finite difference equations are solved numerically making use of a line-by-line method combined with ADI scheme [14]. At every time increment, a number of iterations are carried out in the solution procedure of the equations. SIMPLE algorithm [15] is used for the computation of pressure correction in the iteration procedure.

At the upstream boundary, inlet flow is assumed to be hydrodynamically steady and fully developed. The profile of the streamwise velocity U is given by the approximation [16] which represents a fully developed laminar flow in a rectangular duct. Other velocity components V and W are set to zero at the inlet, while the fluid is assumed to have a uniform temperature at the inlet. No-slip condition is applied at all wall surfaces. The side walls are treated adiabatic, while the other walls are kept at constant temperature higher than the inlet fluid temperature. At the downstream boundary, velocity and temperature profiles are assumed to obey the boundary layer approximation [17].

A maximum of $160 \times 40 \times 110$ grid points are allocated non-uniformly in the computational domain, with fine concentration in the near-wall regions where large gradients of velocity and temperature are expected. The time increment between two successive time steps is set so that the Courant number for the smallest grid spacing is equal to unity.

Calculations are carried out for several cases of different aspect ratios, AR, i.e., the duct width to the step height ratio, and of different Reynolds numbers, Re, based on the step height and the mean velocity at the inlet. The computational conditions are summar-

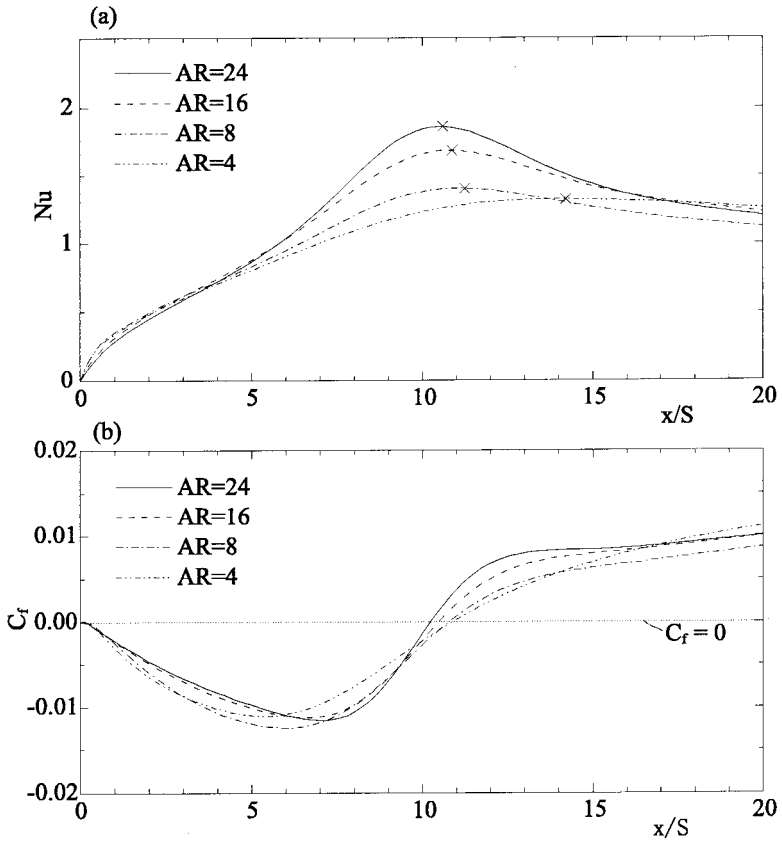

Fig. 2. Nu and C_f distribution along the centerline ($Re = 250$).

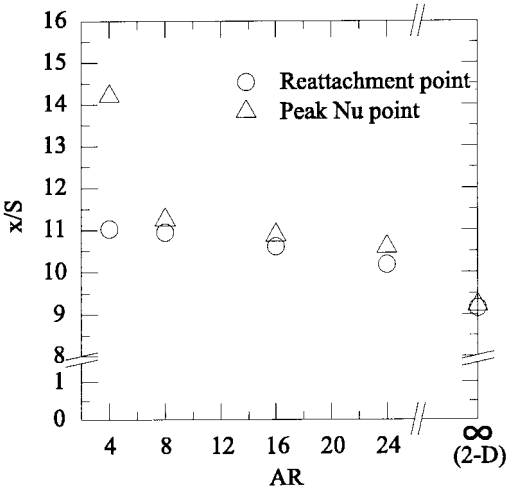

Fig. 3. The effect of AR on the positions of reattachment point and peak Nu point ($Re = 250$).

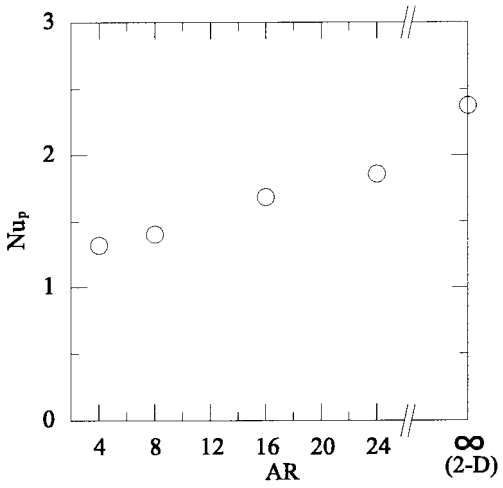

Fig. 4. The effect of AR on the value of peak Nu ($Re = 250$).

ized in Table 1. Numerical results are shown in the following sections for both of laminar and transitional flows in the Reynolds number range of $125 \leq Re \leq 375$. The computed flows were found to remain steady in all the cases calculated here, except in the case of $Re = 375$, in which the flow was found to be periodically unsteady. Distribution will be shown of the time averaged result for the case of $Re = 375$.

Close attention is paid to the distribution patterns of both skin friction coefficient and Nusselt number on the bottom wall.

All calculations were performed on the VP2600 computer at the Kyoto University Data Processing Center. One iteration requires approximately 0.6 s when the total number of grid points is about 4×10^5.

3. Results and discussion

In experimental studies, various characteristic quantities of the fluid flow including Nusselt number, Nu, and streamwise skin friction coefficient, C_f, in the duct are often measured along the streamwise centerline of the bottom wall. A large aspect ratio is often adopted to ensure the two-dimensionality of flow field. Thus, in this study, first will be discussed the effects of the aspect ratio, AR, on the distribution patterns of both Nu and C_f along the centerline. Fig. 2 shows the Nu and C_f distributions along the centerline in the cases of $AR = 4$, 8 and 16, compared with the one in the case of $AR = 24$ (solid line) in which three-dimensionality is expected to be minimum among these four cases. The Reynolds number, Re, is fixed at 250 in these cases. In Fig. 2(a), the peak value of Nu in each case is marked with $\times$. Although the case of $AR = 16$ shows better agreement with the case of $AR = 24$ than the rest of the cases in this figure, it still shows unnegligible deviation in the region of $7 \leq x/S \leq 15$. The maximum difference of 11% between the case of $AR = 16$ and the case of $AR = 24$ is observed in the values of Nu. It is also found in Fig. 2(a) that the peak Nusselt number ($\times$), the highest value of Nusselt number along the centerline of the bottom face, becomes larger and its location moves upstream, as the aspect ratio is increased. In Fig. 2(b), the position where the value of C_f equals to zero around $x/S \simeq 10$ corresponds to the flow reattachment point in each case. C_f distribution also shows the dependency on the value of AR similar to the distribution of Nu. The shape of C_f distribution becomes closer to the one for $AR = 24$ as AR increases. However, maximum difference of 10% is still observed between the two cases $AR = 16$ and $AR = 24$ in the value of C_f. This result suggests that a considerably large aspect ratio is actually needed in order to assume the two-dimensionality of the flow.

The positions of the peak Nu and the flow reattachment are plotted in Fig. 3 together with the result of 2D simulation ($AR = \infty$). The flow reattachment point is defined as the point at which the skin friction coefficient changes its sign from negative to positive. Relative location of these two points has frequently been discussed in turbulent flows, but it has little been discussed in laminar backward-facing step flow. Fig. 3 reveals that both positions shift upstream as AR increases and that the peak Nu position always appears downstream of the reattachment point in 3D simulations. The distance between the peak Nu position and the reattachment point is relatively smaller for a larger aspect ratio, although the distance between the two points still remains finite in the case of $AR = 24$. In 2D simulation, on the other hand, these two points

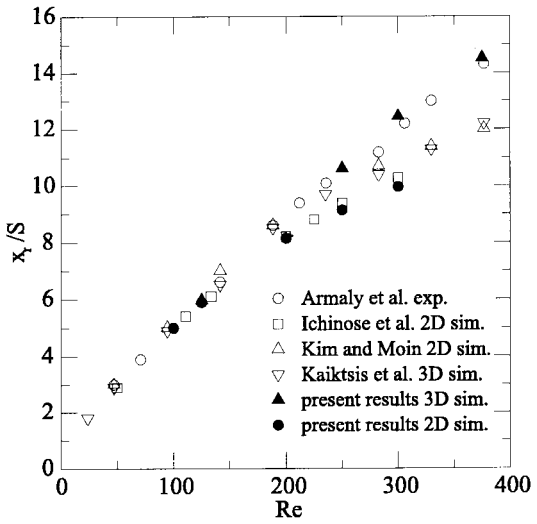

Fig. 5. Reattachment points.

almost coincide at $x/S \simeq 9.2$ and the distance between these two points is less than the grid resolution around this streamwise location. Fig. 4 shows the effect of AR on the value of peak Nusselt number. It is seen that the peak Nusselt number increases as AR is increased.

The evolvement of velocity profiles along the duct centerline, in particular the position of flow reattachment point, obtained from the present calculations agrees well with the experimental counterpart obtained by other researchers [7]. Fig. 5 shows the position of the flow reattachment point plotted against the Reynolds number. Aspect ratio is set equal to 16, commonly, in the present 3D simulations. The position of the reattachment point for $Re = 375$ is its time-averaged value, since the flow in that case became periodically changing unsteady one. As clearly shown here, for a Reynolds number range of $Re < 200$, the present results as well as all the other numerical results reported by Ichinose et al. [9], Kim and Moin [10] and Kaiktsis et al. [11] show good agreement with the experimental results obtained by Armaly et al. [7]. As Reynolds number increases, underestimation of the numerically calculated reattachment length gradually becomes more noticeable, except for the numerical results of the present 3D computation. Results by Kaiktsis et al. [11] plotted in Fig. 5 was obtained by 3D simulations by making use of periodical boundary condition in the spanwise direction, not taking account of the side wall effects. Neglecting the side wall effects must be one of the reason for their tendency similar to the ones of other 2D simulations.

Close attention is paid to the distribution patterns of both the Nusselt number and the skin friction coefficient at the bottom wall surface. Fig. 6 shows the Nusselt number distributions at the bottom wall surface for the cases of different aspect ratios at constant Reynolds number, $Re = 250$. The gray tone level corresponds to the level of the calculated Nusselt number. The gap between two neighboring contourlines is 1/20 of the difference between the maximum and minimum values of the colorbar in all the contour plots in this paper (e.g., 0.25 in Fig. 6). Fig. 6 reveals that the aspect ratio has a great influence on the Nusselt number distribution pattern. An aspect ratio as large as $AR = 16$ at least is needed to obtain a 2D area around the centerline of the bottom wall in the case of $Re = 250$. The 2D area mentioned here is defined as the area where the Nu or C_f contour lines lie parallel to the spanwise direction (z-axis). The 2D area covers 30% of the spanwise width of the bottom wall in the middle at $x/S = 8.0$ for the case of $AR = 16$, and 50% for the case of $AR = 24$. At the positions of $x/S > 10$, however, a three-dimensionality is observed to exist over the whole duct width even for the case of $AR = 16$, as seen in Fig. 6. It is also found that the maximum Nusselt number, Nu_{max} appears near the both side walls, not on the centerline of the bottom wall, in all the cases studied here. With a change of the aspect ratio, change occurs in the location where Nu_{max} is obtained and its value. The locations and values of Nu_{max} calculated in each case are tabulated in Table 2. It is found that Nu_{max} shifts upstream and its value increases as AR increases, while its spanwise location comes close to approximately one step height apart from the both side walls.

Distributions of streamwise skin friction coefficient are shown in Fig. 7, corresponding to ones of Nu shown in Fig. 6. Shaded area in the figure corresponds to the area where the skin friction coefficient is positive

Table 2
Locations and values of Nu_{max} ($Re = 250$)

AR	x_{max}/S	$\lvert z_{max}/WD \rvert$	Distance from a side wall $(WD/2 - \lvert z_{max} \rvert)/S$	Nu_{max}
4	9.5	0.31	0.76	1.9
8	8.9	0.39	0.88	2.7
16	8.1	0.44	0.96	3.4
24	7.5	0.46	0.96	3.6

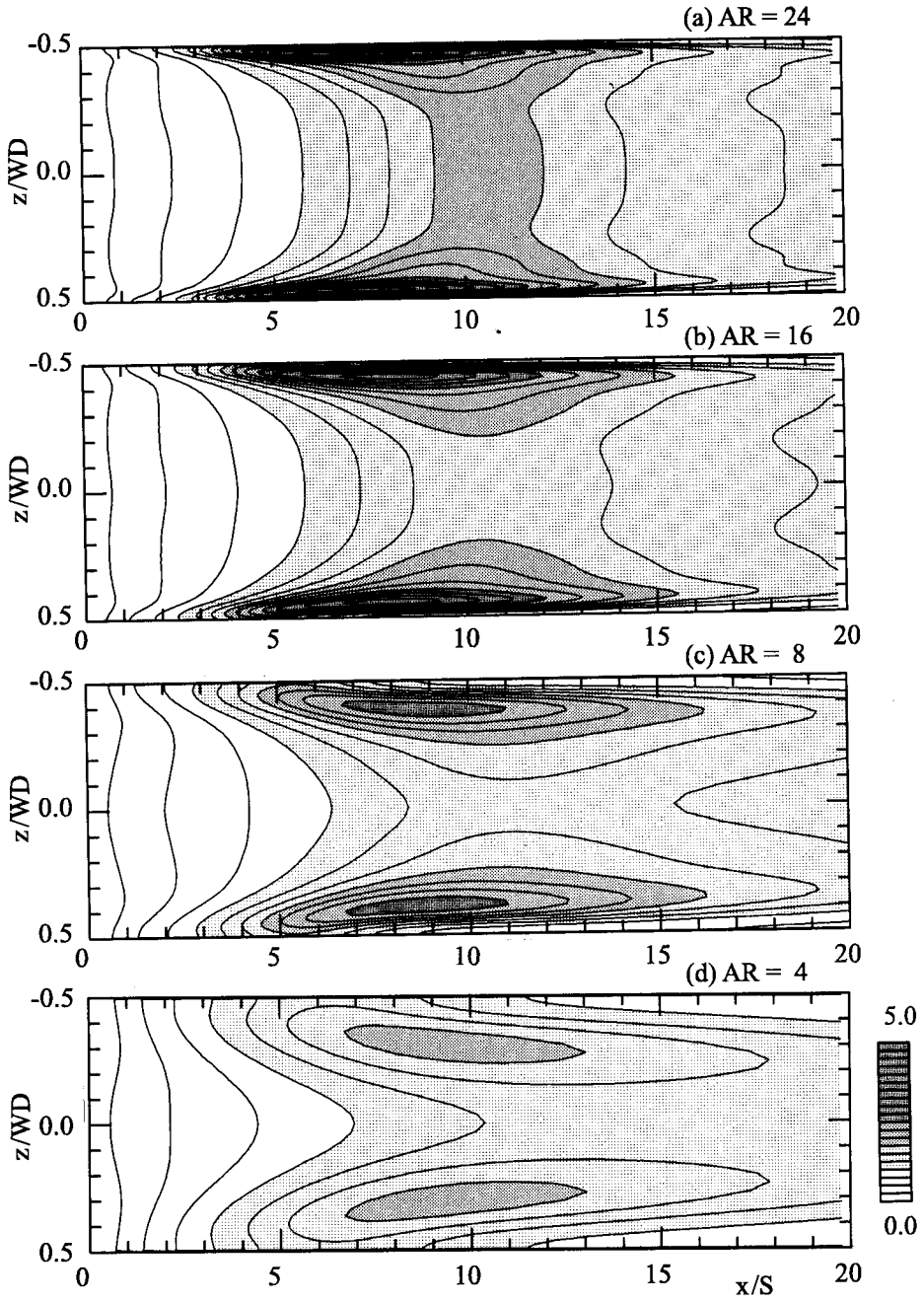

Fig. 6. Nusselt number contours on the bottom wall ($Re = 250$).

in its sign. Being analogous to the case of the Nusselt number distributions mentioned above, an aspect ratio as large as $AR = 16$ at least is needed to assume the two-dimensionality for the distribution of skin friction coefficient in the central region of the duct. The spanwise width of 2D area is about 30% of the duct width at $x/S = 8.0$ for the case of $AR = 16$, and 50% for the case of $AR = 24$.

To discuss the three-dimensionality of the flow and thermal fields in detail, profiles of the flow velocity and temperature in the y–z cross-sections of the duct are examined at three streamwise locations for the case of

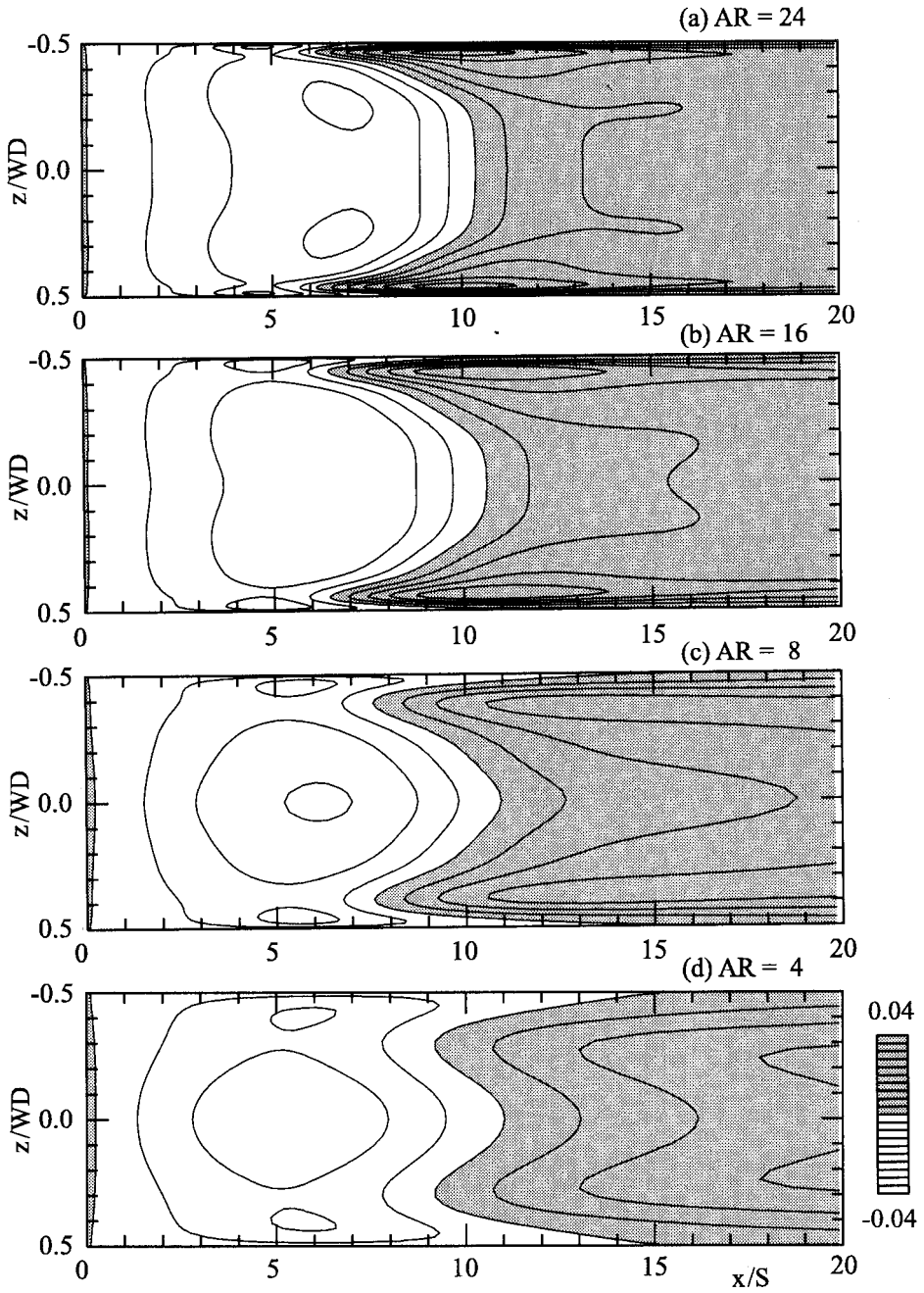

Fig. 7. C_f contours on the bottom wall ($Re = 250$).

$AR = 8$ at $Re = 250$. Fig. 8 shows the upstream view of the velocity vectors (V, W) together with the contours of the streamwise velocity U in three cross-sections of different streamwise positions. Shaded areas in the figures correspond to the positive U velocity regions and white areas to negative U. Fig. 9, on the other hand, shows the profiles of the temperature contours similar to those for velocity contours shown in Fig. 8. Thicker tone correspond to the higher temperature in these figures.

In Fig. 8, it is seen that main flow bends toward the bottom wall after passing the step. Its manner is not uniform in spanwise direction. U contours protrude toward the bottom wall around $|z/WD| \simeq 0.4$. This

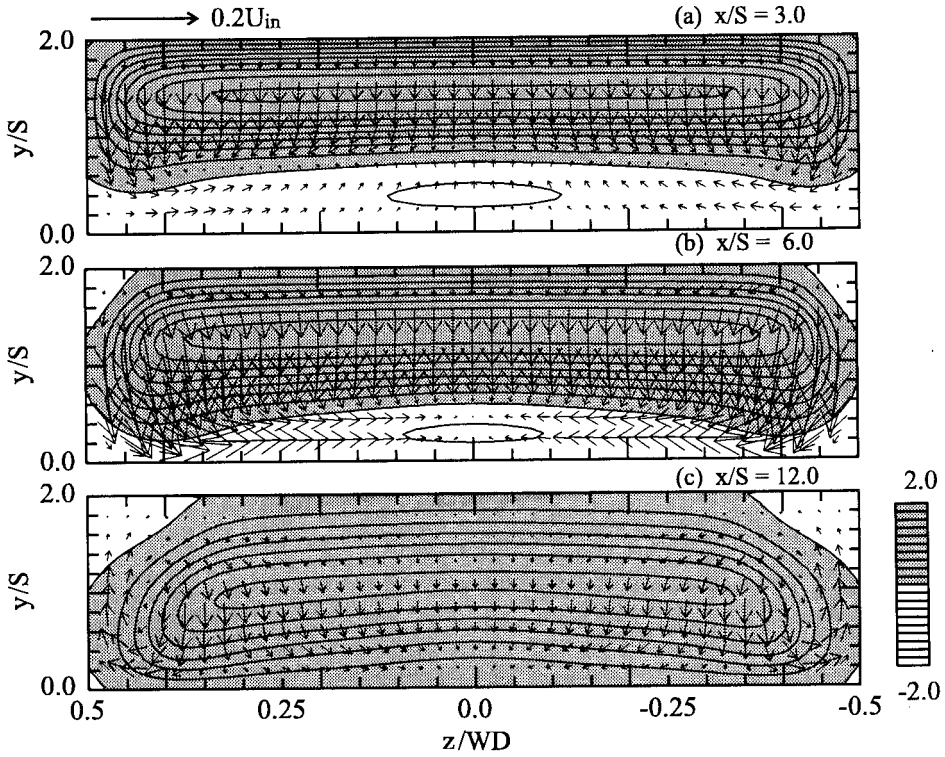

Fig. 8. U/U_{in} contours and V–W vector plots ($Re = 250$, $AR = 8$).

certainly matches the distribution pattern of the streamwise skin friction coefficient. In Fig. 7, upstream indent is also observed in its zero value contour around $|z/WD| \simeq 0.4$. This spanwise non-uniformity of U contours is produced by the downwash flow observed in the middle height region of the channel at corresponding spanwise positions. This is ascribed to the superposition of the secondary flows to the spanwisely uniform downward flow toward the bottom wall. The existence of the secondary flows is clearly confirmed by the upstream view of the velocity vectors (V, W). In Fig. 8, existence of a counter-clockwise rotating flow is observed by the appearance of the flow directed toward the duct center near the bottom wall on the left-hand side ($z/WD > 0$) of the figure at $x/S = 6.0$, while another longitudinal vortex like flow rotating clockwisely is observed at around $z/WD = 0.42$ at $x/S = 12.0$.

The contours of fluid temperature also protrude toward the bottom wall at positions around $|z/WD| \simeq 0.4$ in Fig. 9(b). This corresponds to the velocity profiles shown in Fig. 8(b). Higher spatial density of the contours observed at such spanwise positions near the bottom wall leads to larger temperature gradient there, and, therefore, to larger Nusselt number observed in Fig. 6.

In order to examine the effect of the secondary flows on the heat transfer enhancement from the bottom wall, the value of spanwise skin friction coefficient, Wy at the bottom wall surface defined below is calculated.

$$Wy = \frac{2\mu \left.\frac{\partial W}{\partial y}\right|_{y=0}}{\rho U_{in}^2}$$

where W is the spanwise velocity component. Fig. 10 shows the distribution of Wy contours on the bottom wall. Shaded parts correspond to the regions where the value of Wy is positive in sign while white parts to negative. Wy changes its sign at the centerline of the duct, $z = 0$. This reflects the spanwise symmetry of the flow with respect to the duct centerline. $|Wy|$ are observed to take peaks around the positions $(x/S, z/WD) = (6.5, \pm 0.35)$ and $(11.0, \pm 0.4)$ in the cases of $AR = 8$. The former peaks correspond to the inward flow produced by the rotating secondary flow observed in Fig. 8(b). The latter peaks, on the other hand, correspond to the longitudinal vortex like flow observed at such spanwise positions in Fig. 8(c). Boundary between the shaded and white areas extending from the both side rim of the bottom wall around $x/S = 4$ is observed between these two peaks. The pos-

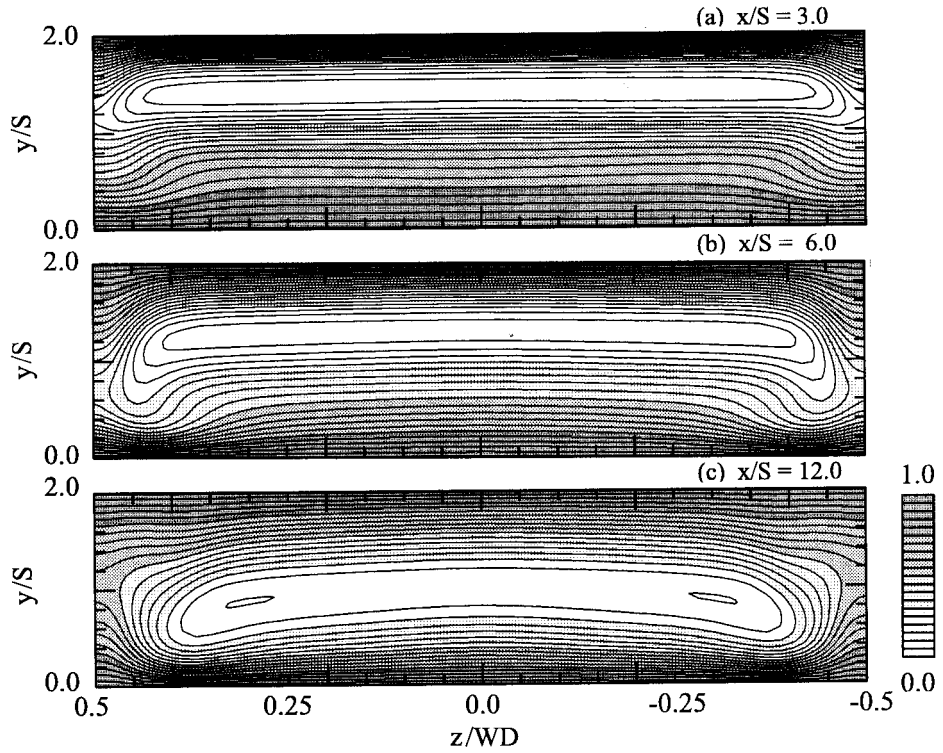

Fig. 9. Normalized temperature $((T - T_{in})/(T_w - T_{in}))$ contours ($Re = 250$, $AR = 8$).

ition of this boundary in the area of $5 < x/S < 10$ coincides with the area where relatively larger value of Nusselt number is observed in Fig. 6. The contour lines of Wy around this boundary become more closely located as the aspect ratio is increased. This means the intensification of the secondary flows, which directly affects the value of Nu_{max} as can be seen in Table 2.

The intersection points of the boundaries between the shaded and white areas in Fig. 7 and the boundaries in Fig. 10 are the stagnation points on the bottom wall where the gradients of both the streamwise velocity, U, and the spanwise velocity, W, are zero. In all the cases studied, a pair of stagnation points are symmetrically obtained with respect to the duct centerline near the both side walls. This is clearly seen in Fig. 11 which shows the velocity vectors (U, W) together with the contours of the normalized absolute value of the local velocity at $y/S = 1.25 \times 10^{-3}$ for the case of $AR = 8$. Fig. 11(b) is a partial enlarged view over region of $5 \leq x/S \leq 15$ and $0 \leq z/WD \leq 0.5$ of Fig. 11(a). Thicker tone correspond to the higher velocity area. Low velocity regions are symmetrically observed near both side walls. The positions of these near side wall stagnation points are calculated in each case and are tabulated in Table 3. Comparison of Tables 2 and 3 reveals that the positions of the stagnation points do not match the positions of the maximum Nusselt number points. Nu_{max} are obtained downstream of the stagnation points.

Fig. 12 shows the influence of the Reynolds number on the Nusselt number distribution. Aspect ratio is kept constant at 16. The spanwise width of the region

Table 3
Locations of near side wall stagnation points ($Re = 250$)

AR	x/S	$\lvert z/WD \rvert$
4	9.2	0.31
8	7.9	0.42
16	6.7	0.46
24	6.4	0.48

Table 4
Locations and values of Nu_{max} ($AR = 16$)

Re	x_{max}/S	$\lvert z_{max}/WD \rvert$	Nu_{max}
125	4.7	0.45	2.1
250	8.1	0.44	3.4
300	9.1	0.44	3.9
375	10.8	0.44	4.7

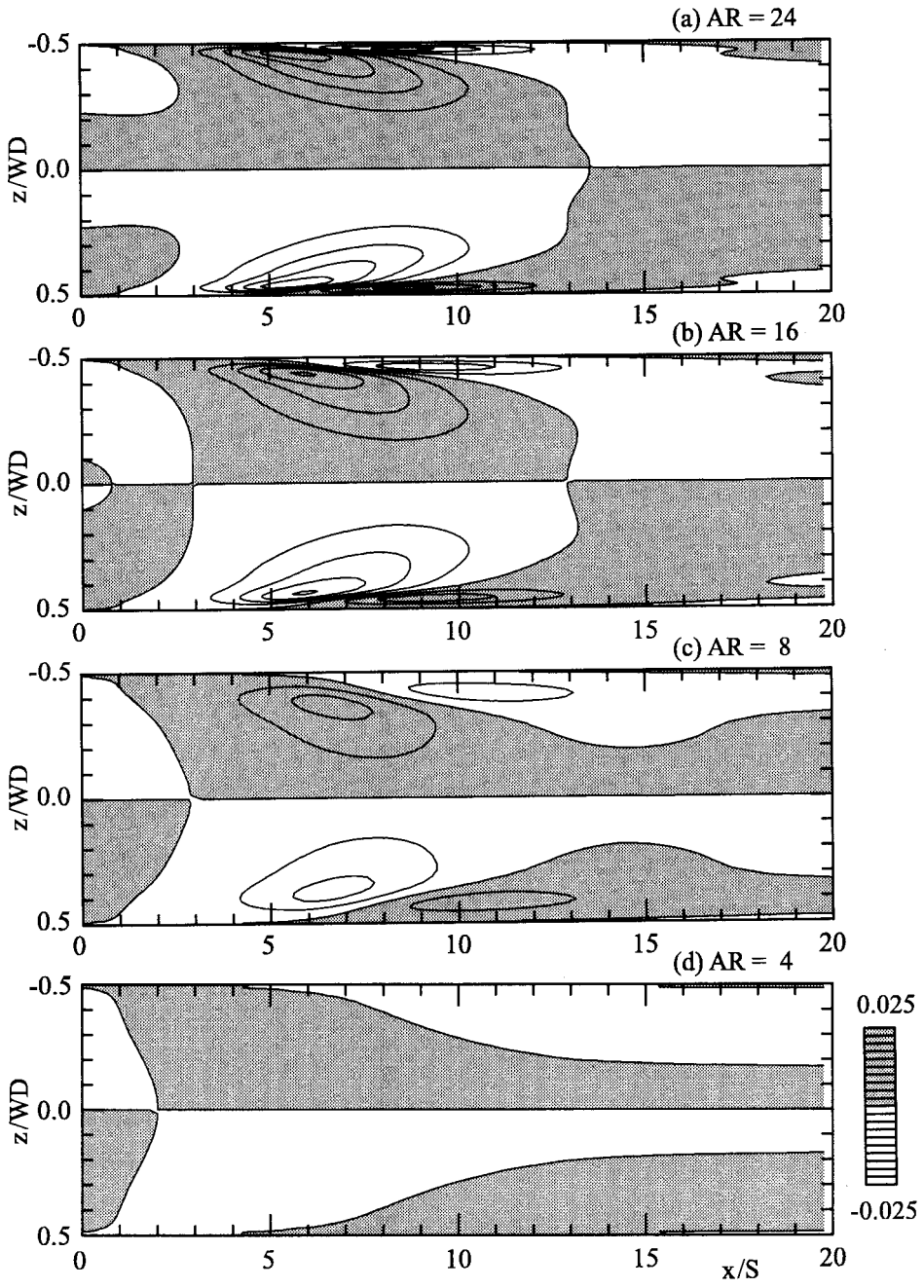

Fig. 10. *Wy* contours on the bottom wall ($Re = 250$).

where two-dimensionality of the thermal field is expected to exist becomes smaller as the Reynolds number is increased. At $x/S = 8.0$, for example, the two-dimensionality is estimated to exist in the middle 50% and 30% of the total spanwise width of the bottom wall, respectively, for the cases of $Re = 125$ and 250. For $Re \geq 300$, however, the 2D region cannot be identified from the distributions of Nusselt number. The locations and the value of the maximum Nusselt number are summarized in Table 4. As the Reynolds number is increased, the maximum Nusselt number becomes larger and its streamwise location shifts downstream. The spanwise location of Nu_{max}, however, does not move so much. This is ascribed to the charac-

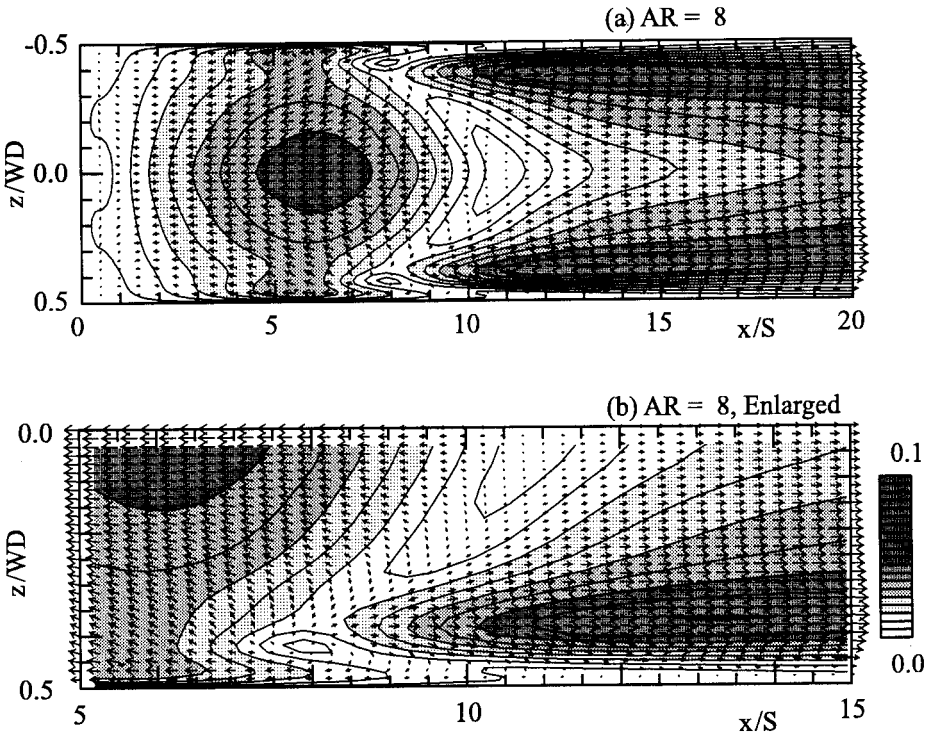

Fig. 11. U–W vector plots with normalized absolute velocity ($\sqrt{U^2 + W^2}/U_{in}$) contours ($Re = 250$, $AR = 8$, $y/S = 1.25 \times 10^{-3}$).

teristics of the secondary flows. Its cross-sectional size does not change but its intensity changes as the Reynolds number is increased.

Fig. 13 shows the C_f distribution for the cases corresponding to those of Fig. 12. Again the spanwise width of the 2D region becomes smaller as Re is increased. In all the cases, the near side wall stagnation points are symmetrically obtained near the positions of Nu_{max} similar to the cases when AR is changed at constant Re. The positions of the near side wall stagnation points are summarized in Table 5. Here again the positions of the near wall stagnation points do not match the positions of the maximum Nusselt number points. Nu_{max} are obtained downstream of the stagnation positions.

In order to visualize the 3D flow pattern, the trajectories of fluid particles tracking the flow are sampled at every constant time interval. Fig. 14 shows a bird's-eye upstream view of the results for the case of $AR = 16$ and $Re = 250$. The top and both side walls of the computational domain are not drawn in this figure. The initial locations of the particles are shown in Table 6. The particles No. 1 and 5, starting from the vicinity of a side wall, are found to recirculate spirally in the recirculating zone behind the step and to move toward the center of the duct, and finally to flow out toward further downstream. The streamwise stroke of the particle extends downstream as the particle approaches the centerline. Therefore, time period for one stroke of particle recirculation becomes longer. This numerical result agrees well with the experimental results obtained by Goldstein et al. [5]. The trajectory patterns and the number of the spiral recirculation strongly depend on the initial location of the particles.

Table 5
Locations of near side wall stagnation points ($AR = 16$)

Re	x/S	$\lvert z/WD \rvert$
125	4.5	0.46
250	6.7	0.46
300	7.4	0.46
375	8.3	0.46

Table 6
Starting locations of the particles

No.	1	2	3	4	5
x/S	0.0	0.0	0.0	0.0	0.0
y/S	1.04	1.30	1.04	1.04	1.04
z/WD	0.47	0.30	0.00	−0.40	−0.48

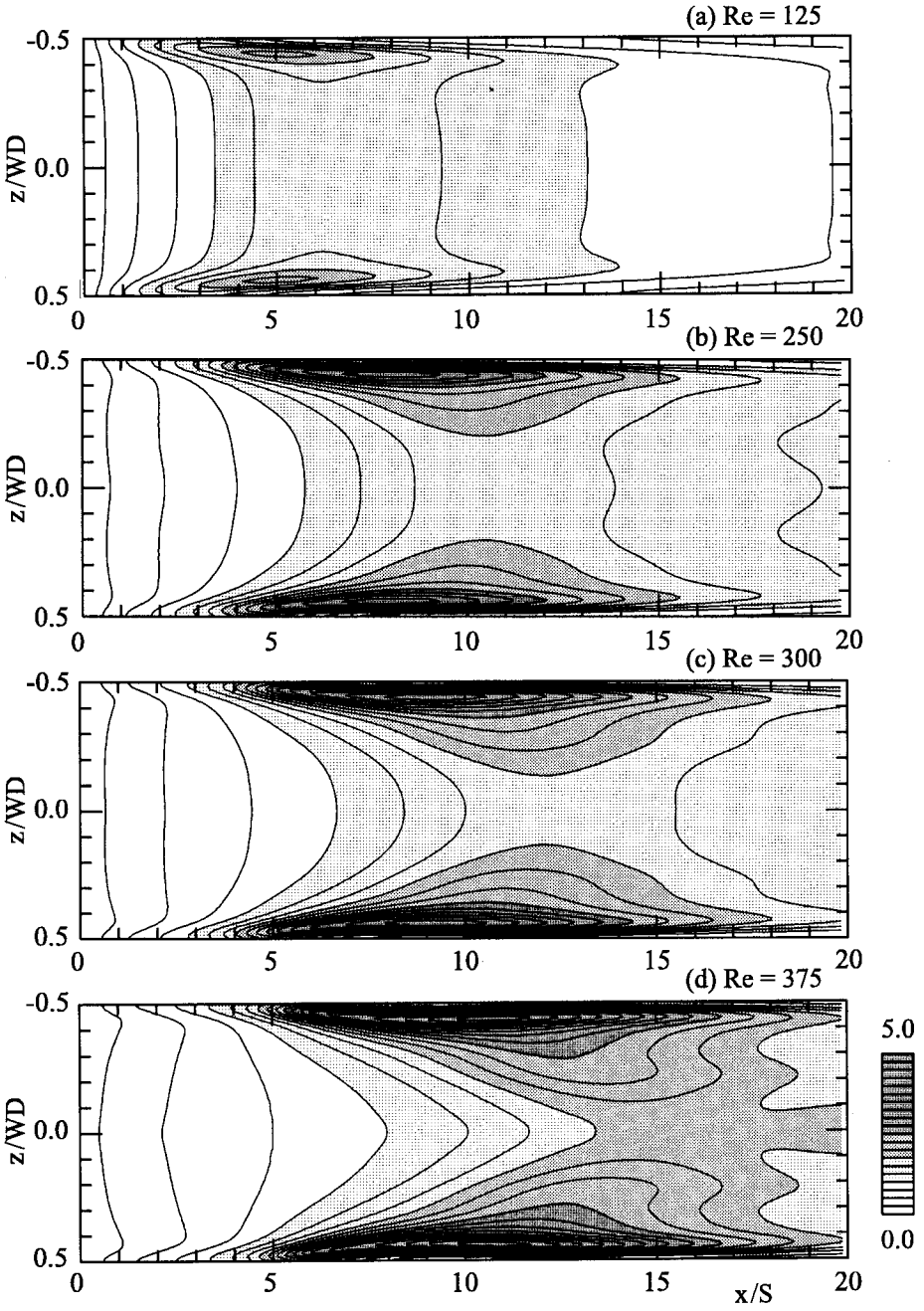

Fig. 12. Nusselt number contours on the bottom wall ($AR = 16$).

This method of presentation of the results was proven effective to visually examine the three-dimensionality of the flow.

In relation with the above mentioned interesting spiral motion of the particles, pressure distributions are calculated in the vicinity of the bottom wall. Fig. 15 shows the pressure coefficients along the centerline of the bottom wall in the case of $AR = 16$ and $Re = 250$. The reference pressure is its value at a position near the origin of the coordinate system. Spanwise non-uniformity of pressure is also examined introducing the non-dimensional pressure non-uni-

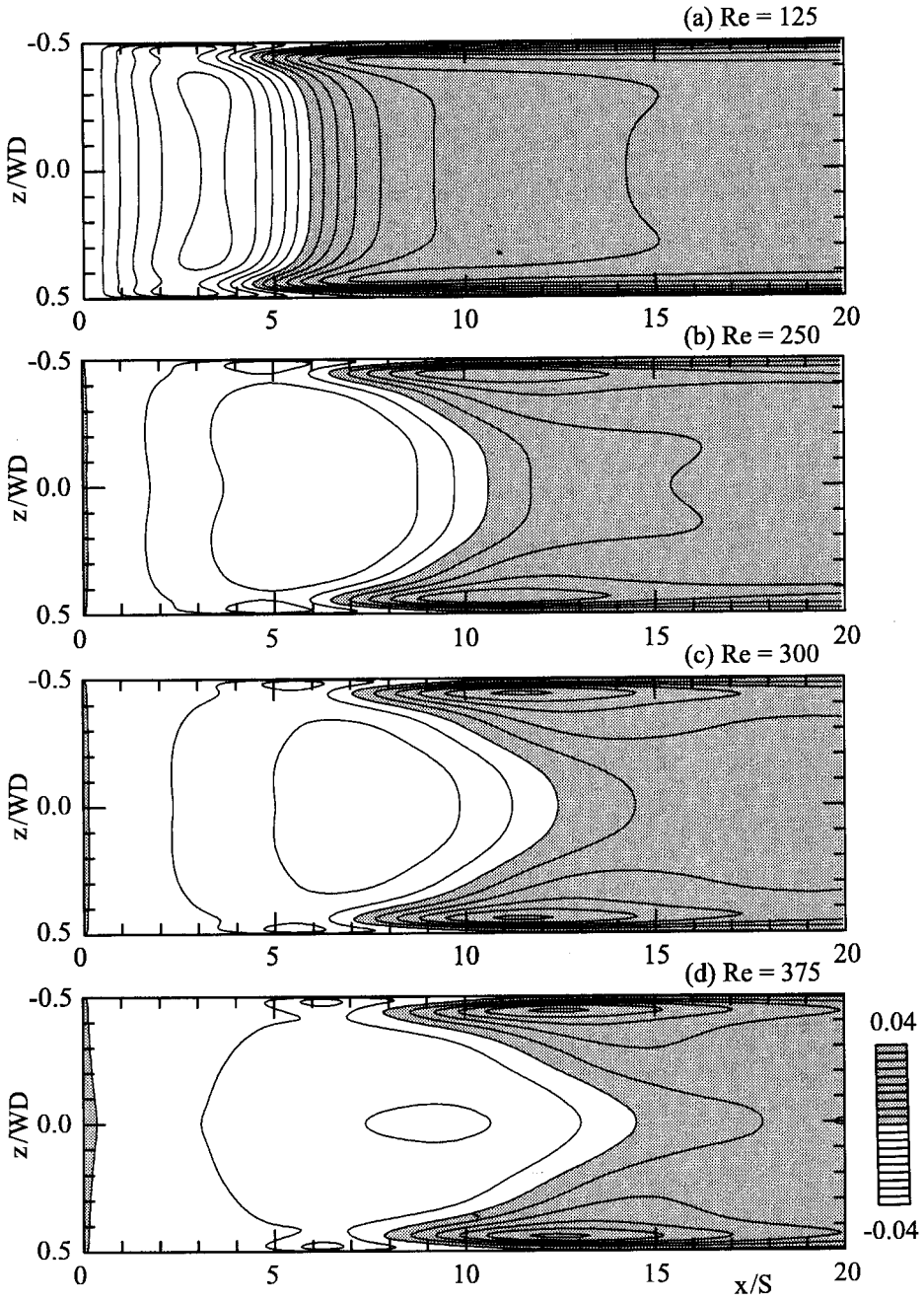

Fig. 13. C_f contours on the bottom wall ($AR = 16$).

formity, $C_{p,z}$ which is calculated using the centerline pressure at respective streamwise position as its reference value. The results are shown in Fig. 16. Shaded areas indicate that the value of $C_{p,z}$ is positive in sign. $C_{p,z}$ is zero along the boundary between the shaded area and the neighboring white area, and also along the centerline. Spanwise pressure gradient is noticeable near the side wall, although less profound in the middle 40% region of the duct width. The spiral fluid motion in the recirculating flow region was found to approach toward the center of the duct. This is caused by this spanwise pressure non-uniformity decreasing

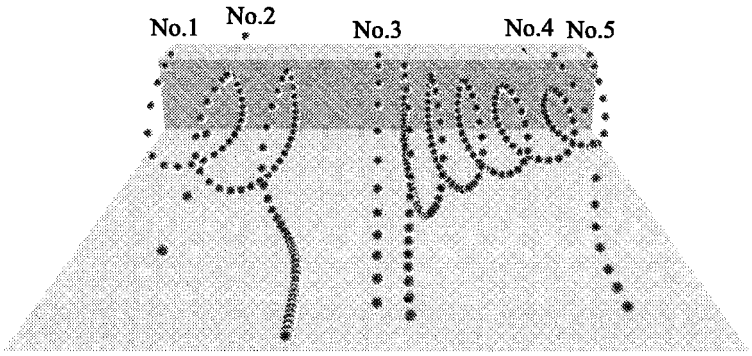

Fig. 14. Behavior of fluid particles ($Re = 250$, $AR = 16$).

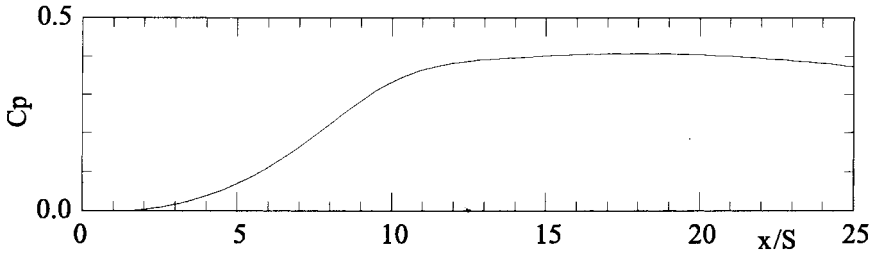

Fig. 15. C_p distribution along the centerline ($Re = 250$, $AR = 16$).

toward the centerline. The maxima of $C_{p,z}$ are symmetrically located near the both side walls at approximately $x/S = 6.7$ and $|z/WD| = 0.45$.

4. Conclusions

Three-dimensional numerical simulation has been performed for the laminar flows over a backward-facing step in a rectangular duct. The results obtained in the present study are summarized as follows:

1. Flow reattachment points calculated in the present study agree well with the existing experimental results.
2. An aspect ratio of as large as $AR = 16$ at least is needed to secure 2D region in the central part of the duct at a Reynolds number of $Re = 250$. In the case of constant aspect ratio, $AR = 16$, the area of the 2D region becomes larger, as Re number is decreased.
3. The maximum Nusselt number on the bottom wall is obtained at two positions near the side walls located symmetrically with respect to the duct centerline, and not on the centerline in all the cases

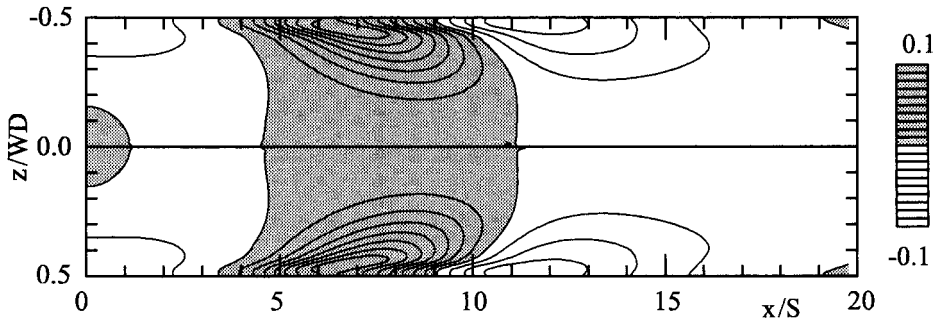

Fig. 16. $C_{p,z}$ contour on the bottom wall ($Re = 250$, $AR = 16$).

studied here. It is also found that the maximum Nusselt number increases with an increase of the aspect ratio and Reynolds number.

4. The particles starting from the vicinity of a side wall are found to recirculate spirally in the recirculating zone behind the step. This spiral fluid motion in the recirculating flow region approaches toward the center of the duct because of the spanwise pressure non-uniformity decreasing toward the centerline.

References

[1] M. Fiebig, P. Kallweit, N.K. Mitra, Wing type vortex generators for heat transfer enhancement, Proc. 8th Int. Heat Transfer Conf 6 (1986) 2909–2913.

[2] M. Fiebig, Vortex generators for compact heat exchangers, J. Enhanced Heat Transfer 2 (1–2) (1995) 43–61.

[3] R.L. Webb, E.R.G. Eckert, R.J. Goldstein, Heat transfer and friction in tubes with repeated-rib roughness, Int. J. Heat Mass Transfer 14 (1971) 601–617.

[4] G.L. Lehmann, R.A. Wirtz, Effect of variations in streamwise spacing and length on convection from surface-mounted rectangular components, Heat Transfer Eng 9 (3) (1988) 66–75.

[5] R.J. Goldstein, V.L. Ericsen, R.M. Olson, E.R.G. Eckert, Laminar separation, reattachment, and transition of the flow over a downstream-facing step, J Basic Eng. 92 D(4) (1970) 732–741.

[6] M.K. Denham, M.A. Patrick, Laminar flow over a downstream-facing step in a two-dimensional flow channel, Trans. Instn. Chem. Engrs 52 (1974) 361–367.

[7] B.F. Armaly, F. Durst, J.C.F. Pereira, B. Schonung, Experimental and theoretical investigation of backward-facing step flow, J. Fluid Mechanics 127 (1983) 473–496.

[8] B.J. Baek, B.F. Armaly, T.S. Chen, Measurements in buoyancy-assisting separated flow behind a vertical backward-facing step, Trans. ASME: J. Heat Trans 115 (1993) 403–408.

[9] K. Ichinose, H. Tokunaga, N. Satofuka, Numerical simulation of two-dimensional backward-facing step flows, Trans. JSME B 57-543 (1991) 3715–3721.

[10] J. Kim, P. Moin, Application of a fractional-step method to incompressible Navier–Stokes equations, J. Computational Physics 59 (1985) 308–323.

[11] L. Kaiktsis, G.E. Karniadakis, S.A. Orszag, Onset of three-dimensionality, equilibria, and early transition in flow over a backward-facing step, J. Fluid Mech 231 (1991) 501–528.

[12] J.T. Lin, B.F. Armaly, T.S. Chen, Mixed convection in buoyancy-assisting, vertical backward-facing step flows, Int. J. Heat Mass Transfer 33-10 (1990) 2121–2132.

[13] J.T. Lin, B.F. Armaly, T.S. Chen, Mixed convection heat transfer in inclined backward-facing step flows, Int. J. Heat Mass Transfer 34 (6) (1991) 1568–1571.

[14] P.J. Rocache, Computational Fluid Dynamics, Hermosa Publishers, Albuquerque, 1976.

[15] S.V. Patankar, D.B. Spalding, A calculation procedure for heat, mass and momentum transfer in three-dimensional parabolic flows, Int. J. Heat Mass Transfer 15 (10) (1972) 1787–1806.

[16] R.K. Shah, A.L. London, Laminar Forced Convection in Ducts, Academic Press, New York, 1978.

[17] S. Kieda, K. Suzuki, Numerical study of the flow passing a flat plate of finite length, Trans. JSME B 46 (409) (1984) 1655–1661.